


Fundamental Parameters for Totally Eclipsing Contact Binaries Observed by TESS

XU DING ^{1,2,3}, KAIFAN JI,^{1,2,3,4} ZHIMING SONG,^{5,6} XUEFEN TIAN,⁷ JINLIANG WANG,^{1,2,3,4} CHUANJUN WANG,^{1,2,3,4}
QIYUAN CHENG,^{1,2,3,4} AND JIANPING XIONG^{1,2,3}

¹Yunnan Observatories, Chinese Academy of Sciences (CAS), P.O. Box 110, 650216 Kunming, P. R. China

²Key Laboratory of the Structure and Evolution of Celestial Objects, Chinese Academy of Sciences, P. O. Box 110, 650216 Kunming, P. R. China

³Center for Astronomical Mega-Science, Chinese Academy of Sciences, 20A Datun Road, Chaoyang District, Beijing, 100012, P. R. China

⁴University of the Chinese Academy of Sciences, Yuquan Road 19#, Shijingshan Block, 100049 Beijing, P.R. China

⁵School of Information, Yunnan University of Finance and Economics, Kunming, China.

⁶Yunnan Key Laboratory of Service Computing, Kunming, China.

⁷Communication And Information Engineering College, Yunnan Open University, 650500 Kunming, P. R. China

ABSTRACT

Totally eclipsing contact binaries provide a unique opportunity to accurately determine mass ratios through photometric methods alone, eliminating the need for spectroscopic data. Studying low mass ratio (LMR) contact binaries is crucial for advancing our understanding of binary star evolution and the formation of rare optical transients known as red novae. We identified 143 totally eclipsing contact binaries from TESS. These high-precision light curves reveal a distinct O’Connell effect, which we interpret by introducing a cool spot on the primary star. Training a neural network model that includes a cool spot parameters can generate a high-precision light curve two orders of magnitude faster than Phoebe. Utilizing the neural network (NN_{no13}) model combined with the Markov Chain Monte Carlo (MCMC) algorithm, we rapidly derived the fundamental parameters of these systems. By leveraging the relationship between orbital period and semi-major axis using Random Sample Consensus (RANSAC) algorithm, we estimated their absolute parameters. Our analysis identified 96 targets with mass ratios below 0.25, all of which were not listed in any previous catalog, thus signifying the discovery of new low mass ratio system candidates. Assuming all 143 binary systems are affected by a third light during parameter estimation, we train a neural network (NN_{l3}) model considering the third light. Then we calculate the residuals between the mass ratio q_{l3} (considering the third light) and q_{no13} (neglecting it). For these residuals, the 25th percentile (Q_1) is 0.012, the median (Q_2) is 0.026, and the 75th percentile (Q_3) is 0.05.

Keywords: Binary stars (154) — Eclipsing binary stars(444) — Contact binary stars(297)

1. INTRODUCTION

The two component stars in a contact binary system are completely within their respective Roche lobes (Kopal et al. 1959; Lucy et al. 1968a,b), sharing a common envelope and undergoing significant mass exchange (Lucy et al. 1979). Despite potential substantial mass discrepancies between the two stars, their temperatures remain relatively similar (Kuiper et al. 1941). These parameters, including mass ratio, fill-out factor, and temperature ratio, are crucial for understanding the various evolutionary stages of contact binaries (Yakut et al. 2005; Yildiz et al. 2013; Li et al. 2020; Sun et al. 2020; Latković et al. 2021). To accurately determine the fundamental parameters of a contact binary, both photometric light curves and radial velocity data are necessary. Given the necessity of a considerably larger telescope for radial velocity observations compared to photometric studies, only a limited number of contact binaries have their

radial velocities measured. Pribulla et al. (2003) determined that contact binaries displaying flat-bottom minima in their light curves possess photometric mass ratios nearly identical to their spectroscopic counterparts, indicating that total eclipsing contact binaries can achieve reliable mass ratio determinations without spectroscopic data. The behavior of totally eclipsing W UMa systems, as anticipated by the Lucy model, strongly constrains their geometry and the models fitted to their light curves (Mochnicki & Doughty 1972a,b). Reliable mass ratio parameters are essential for identifying contact binaries with low mass ratios. Theoretically, it is suggested that contact binaries exhibit a low mass ratio cutoff and are prone to merging into fast-rotating single stars due to the Darwin instability (Rasio et al. 1995; Li & Zhang et al. 2006; Arbutina et al. 2007, 2009; Jiang et al. 2010; Wadhwa et al. 2021). As of now, the only confirmed merging event involving contact binaries, based on observational data, is that of V1309 Sco (Tylenda et al. 2011).

The proliferation of light curve data from surveys such as the Catalina Sky Survey (CSS) (Marsh et al. 2017), the Kepler mission (Borucki et al. 2010; Koch et al. 2010), and the Transiting Exoplanet Survey Satellite (TESS) (Ricker et al. 2015) has facilitated the identification of total eclipsing contact binaries with low mass ratios (Christopoulou et al. 2022; Lalounta et al. 2024). Notably, Ding et al. (2024) utilized an autoencoder neural network to sift through TESS survey data, uncovering 1322 candidate contact binaries. This catalog provides highly precise light curves of total eclipsing contact binaries observed by TESS. Traditional methods for deriving contact binary parameters, such as the Wilson–Devinney program (Wilson 1990, 2012; Wilson & Devinney 1971; Wilson et al. 2010; Van Hamme & Wilson 2007) and the Phoebe program (Prša et al. 2016), are time-consuming, often requiring hours to days per target. Consequently, the derivation of parameters for a large number of light curves remains a formidable challenge. Machine learning techniques have shown promise in accelerating parameter acquisition for binaries (Prša et al. 2008; Ding et al. 2022; Xiong et al. 2024). However, these methods typically rely on symmetric light curves and do not account for the O’Connell effect (O’Connell et al. 1951; Milone et al. 1968), which refers to asymmetric light curves.

In this study, we introduce a novel approach that establishes a mapping from parameters, including a cool spot parameters, to light curves. We train a neural network (NN_{not3}) model and subsequently employ the Markov Chain Monte Carlo (MCMC) algorithm from the emcee program (Foreman-Mackey et al. 2019) to swiftly obtain the posterior distribution of the parameters. This methodology effectively fits the light curves of contact binaries exhibiting the O’Connell effect. Ultimately, we compile a catalog of 143 total eclipsing contact binary parameters, 96 of which represent newly identified low mass ratio contact binary candidates. Given that all 143 binary systems are impacted by a third light source during parameter estimation, a neural network model (NN_{l3}) incorporating this third light was trained. The mass ratios q_{l3} (considering the third light) and q_{not3} (neglecting it) were compared. The structure of this paper is as follows. Section 2 outlines the sample selection process. Section 3 details the establishment of the neural network model. Section 4 presents the derivation of parameters for the total eclipsing contact binaries. Section 5 includes discussions, primarily comparing our findings with other catalogs. The final section concludes the paper.

2. TESS SAMPLE SELECTION

Ding et al. (2024) employed an autoencoder neural network to search for contact binaries from TESS, successfully identifying 1322 candidate contact binaries. We utilize the Python package `lightkurve`¹ to obtain the TESS light curves authored by SPOC for these targets. We employed the Lomb-Scargle periodogram (Lomb 1976; Scargle 1982) along with the bootstrap (Efron et al. 1979) method to estimate the orbital periods and their associated uncertainties for these targets. The light curves exhibit the O’Connell effect, characterized by unequal brightness levels of the maxima occurring between the eclipses. Therefore, we only folded the light curves for the first three periods. To transform the flux values obtained from TESS into magnitudes, we apply the following formulas.

$$\text{mag}_i = -2.5 \times \log_{10}(\text{flux}_i) \quad (1)$$

$$\Delta \text{mag}_i = \text{mag}_i - \frac{\sum_{i=1}^n \text{mag}_i}{n} \quad (2)$$

where flux_i is the flux obtained from TESS. Δmag_i is the normalized value.

We identified 143 total eclipsing contact binaries among these targets whose light curves exhibit flat-bottom minima. The application of Gaussian Process Regression (GPR)² for accurately fitting the light curve. During the first and

¹ <https://docs.lightkurve.org/>

² <https://github.com/dfm/george/>

second out-of-eclipse phases, the maximum magnitudes are denoted as $Max.I$ and $Max.II$ respectively. Taking TIC 103656297 as an example, its relevant data are presented in the left panel of Figure 1. The results for the 143 targets show that the value of ΔMag , which is calculated as $\Delta Mag = Max.I - Max.II$, is presented in the middle panel of Figure 1. The O’Connell effect of TIC 103656297 changes over time, as shown in the right panel of Figure 1. Late-type contact binary stars usually exhibit relatively strong magnetic activity. The noise of the TESS light curve, which is primarily centered ~ 0.0012 mag, was statistically analyzed by Ding et al. (2024). Under such a low noise level and considering the magnetic activity phenomenon of late-type stars, the ΔMag value clearly indicates the asymmetry of the light curve.

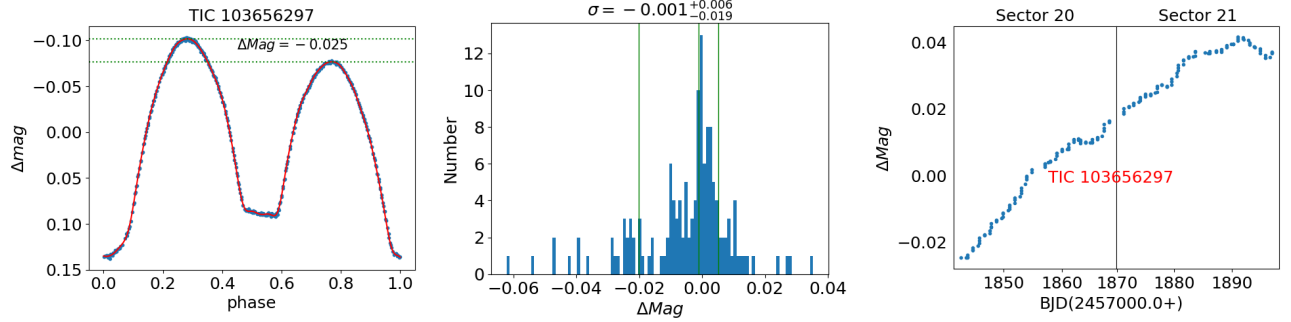


Figure 1. Left: the blue dots depict the original light curve data, while the red line signifies the fitting outcome. The green lines highlight the Max.I and Max.II points within the light curves. Middle: the plot displays the ΔMag distribution specifically for 143 light curves. Right: in Sectors 20 and 21, the O’Connell effect of TIC 103656297 varies with the passage of time.

3. BUILDING A NEURAL NETWORK MODEL

In their analysis of the catalog referenced in Latković et al. (2021), Ding et al. (2024) found that there were a total of 30 published targets recorded for the year 2020. In the light curve fitting of these targets, only BB Peg is particularly noteworthy as it features the addition of two cool spots. For the other targets, the fitting can be accomplished by adding just one cool spot. Therefore, the inclusion of a single cool spot can effectively fit the light curves of most targets. Therefore, we established a mapping relationship between the parameters and the light curves, where the parameters include those of the cool spots. In adherence to Occam’s razor, our approach is to fit the light curve utilizing the minimum number of parameters. This stance, however, does not preclude the potential presence of a third light source, which necessitates an extended observational timeframe to scrutinize variations in the orbital period (O-C) (Zhao et al. 2021). Consequently, our generated dataset omits any consideration of the third light.

3.1. Sample data set

In contact binary systems, the light curve is significantly affected by several key parameters, including the mass ratio (q), orbital inclination ($incl$), effective temperatures of the primary star (T_1) and the secondary star (T_2), fill-out factor (f), gravity-darkening coefficient (g), bolometric albedos (A), and the semi-major axis (sma), as well as the passband and parameters of any cool spots. The characteristics of a cool spot are typically defined by its colatitude ($colat$), longitude ($long$), angular radius ($radius$), and the temperature ratio compared to the local intrinsic value ($relteff$). To obtain accurate light curves for contact binaries, we use the Phoebe program, which relies on these fundamental parameters. The selected passband is TESS:T, which encompasses a broadband wavelength range from 600 to 1000 nm (Ricker et al. 2015). To enhance the sample density, we adopt a random fraction method for generating these light curves.

The mass ratio (q) is distributed within the interval $[0,1]$. The orbital inclination ($incl$) ranges between 50 and 90 degrees. The fill-out factor (f) follows a distribution across the range $[0,1]$. The temperature of the primary star (T_1) is distributed within $[4000K, 8000K]$. The temperature ratio (T_2/T_1) is modeled by a Gaussian distribution with a mean (μ) of 1 and a standard deviation (σ) of 0.2. The colatitude ($colat$) spans the interval $[0,180]$. The longitude ($long$) of the cool spot on the primary star is distributed throughout the range of 0 to 360 degrees. The angular radius ($radius$) ranges from 0 to 50 degrees, and the temperature ratio relative to the intrinsic local value ($relteff$) is distributed within $[0.6,1]$. We maintain Phoebe’s default settings for limb-darkening, using `ld.func=‘interp’` for

the linear interpolation algorithm, and for the reflection effect, we retain `irrad_method='none'`, corresponding to the 'Horvat' method, which is Lambertian. For each local point on a star, the limb-darkened intensity distribution is interpolated from pre-computed tables based on the effective temperature (T_{eff}), surface gravity ($\log g$), metallicity ($[M/H]$), and other relevant physical parameters (Prša et al. 2016). For effective temperatures below 8000K, the gravity-darkening coefficient (g) is set to 0.32, and the bolometric albedo (A) is set to 0.6. The atmosphere model is selected as ck 2004. The semi-major axis (sma) is set to 1, enabling the acquisition of the relative radii of the primary and secondary stars. The dataset comprises 200,000 samples.

Table 1. Parameter Range of Contact Binaries.

Num	parameter	range
1	q	0-1
2	$incl(^{\circ})$	50-90
3	$T_1(K)$	4000-8000
4	T_2/T_1	$\mu = 1, \sigma = 0.2$
5	f	0-1
6	$g_1 = g_2$	0.32
7	$A_1 = A_2$	0.6
8	passband	TESS:T
9	sma	1
10	$colat(^{\circ})$	0-180
11	$long(^{\circ})$	0-360
12	$radius(^{\circ})$	0-50
13	$relteff$	0.6-1

3.2. A neural network model

Neural Network-Based Mapping of Parameters to Light Curves with Phase-Magnitude: A multilayer perceptron (MLP) neural network is utilized to establish the relationship between parameters and light curves, focusing specifically on the phase-magnitude characteristics. For this purpose, we developed a neural network model to aid in the analysis.

The configuration of the neural network we developed is depicted in Figure 2. This architecture primarily comprises an input layer, multiple hidden layers, and an output layer. The values shown in Figure 2 correspond to the number of nodes in each of these layers. The input layer of the model contains 9 nodes, reflecting the 9 input parameters ($T_1, q, incl, f, T_2/T_1, colat, long, radius, relteff$). Activation functions are incorporated into both the input and hidden layers, enabling the resolution of non-linear relationships that cannot be expressed linearly. We opted for the ReLU activation function (He et al. 2015) for both models. The loss function measures the discrepancy between the predicted and actual values of the model. The variation of the loss function on the validation set is used to select an optimal model for further training on the training set. The Mean Square Error (MSE) is chosen as the loss function. The Adam optimizer (Kingma et al. 2014) was selected for the neural network. The model requires approximately 0.01 seconds to generate a light curve with 100 points when executed on a computer equipped with 32G of random-access memory, an i7-8700 CPU operating at 3.20 GHz. Under identical conditions, the Phoebe program takes approximately 5.72 seconds to generate a light curve with 100 points. The speed at which the neural network model generates light curves is two orders of magnitude faster than that of Phoebe. The i7-8700 CPU has 6 cores and can support 12 threads as it allows two threads per core. Both the neural network model and Phoebe were run in single-thread mode when generating light curves based on parameters for the speed comparison. No parallel mode using multiple threads was employed.

3.3. Precision of light curves generated by neural network model

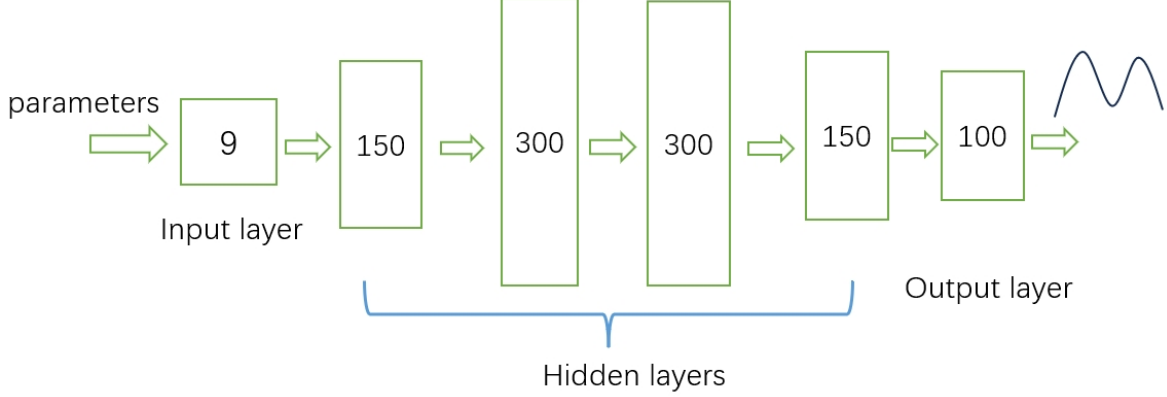


Figure 2. This figure illustrates the structure of the neural network, where the node number represents the count of neurons.

The original dataset is partitioned into three distinct subsets following an 8:1:1 distribution: training, validation, and test sets. The training set is utilized to construct a neural network model, which undergoes a learning process to optimize its parameters. Once the training phase is complete, the resulting model is considered the final iteration. Its effectiveness is then verified through evaluation against the validation set. Finally, the precision with which the model generates light curves is measured by testing it against the independent test set.

The precision of light curves generated by the model is evaluated by examining the standard deviation of the residuals. This assessment involves comparing the distribution of residuals from the synthetic light curves produced by Phoebe with those generated by the model. As depicted in the left panel of Figure 3, the blue light curve was generated by Phoebe using the following input parameters: $T_1 = 7342$ K, $incl = 73.57^\circ$, $q = 0.27$, $f = 0.91$, $T_2/T_1 = 1.01$, $relteff = 0.79$, $colat = 28^\circ$, $long = -95^\circ$, $radius = 11^\circ$. The model, employing the same set of parameters, produced the orange light curve in the same panel. The standard deviation of the residuals between these two curves is calculated to be 0.0005. Additionally, we computed the standard deviation of residuals across a sample of 20,000 light curves. The right panel of Figure 3 illustrates that the standard deviations of the residuals are predominantly distributed around $0.0006^{+0.0003}_{-0.0002}$. While the number of hidden layers and neurons in this work may not be optimal, they suffice to meet the requirements in terms of generating light curve accuracy.

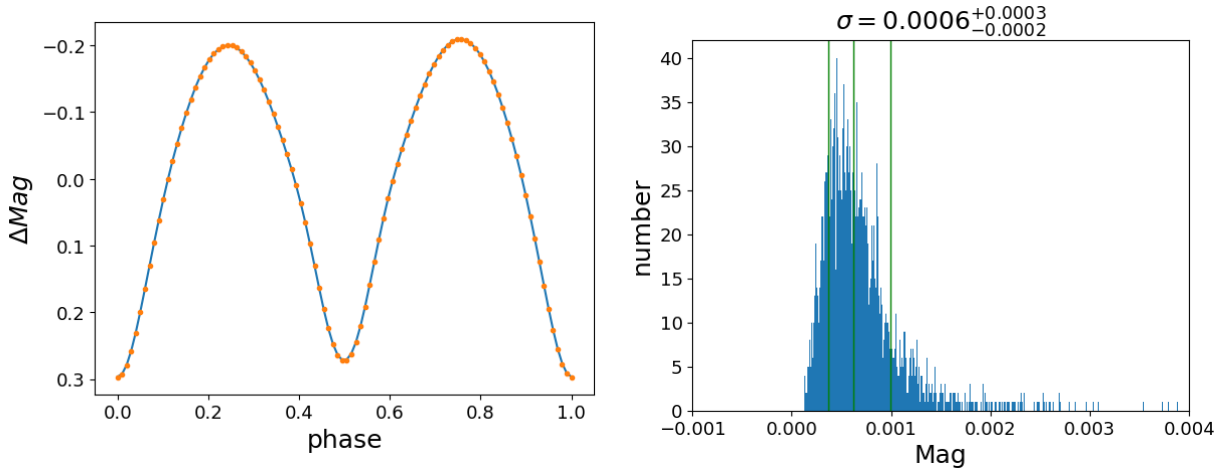


Figure 3. Left: The blue light curve was synthesized by Phoebe, whereas the orange light curve was generated by the model employing the same set of input parameters. Right: The distribution of the standard deviation of the residuals between the predicted light curves produced by the model and the synthetic light curves produced by Phoebe is depicted.

4. TESS SURVEY: CONTACT BINARY PARAMETERS

Employing a neural network (NN_{mol3}) model that has been trained and fine-tuned, in conjunction with the Markov Chain Monte Carlo (MCMC) algorithm, we successfully derive the posterior distributions of the parameters characterizing contact binaries. We then further estimated the absolute parameters of these targets.

4.1. Relative parameters

The relative parameters for 143 contact binaries are determined through the utilization of a neural network (NN_{mol3}) model in conjunction with the Markov Chain Monte Carlo (MCMC) algorithm. An illustrative case is presented using TIC 164720673 to demonstrate the extraction of these parameters for the specific object. Subsequently, the fitting outcomes for four objectives are detailed.

Initially, we employed the NN_{mol3} model along with the MCMC algorithm to derive the posterior distribution of the parameters for the target identified as TIC 164720673. A total of 30 parameter space walkers were utilized. To ascertain the convergence of the MCMC chain, multiple criteria have been established to select an adequate chain length, such as a duration that is 10–20 times the integrated autocorrelation time (Conroy et al. 2020; Li et al. 2021). For contact binaries exhibiting flat-bottom minima in their light curves, a significant proportion are identified as low mass ratio systems. In such systems, the primary component (the hotter star) plays a dominant role in determining the system’s effective temperature, T_{sys} . Hence, for contact binaries with low mass ratios, where the temperature of the primary component largely dictates the system temperature, we consider T_{sys} to be approximately equal to T_1 (the effective temperature of the primary star). The effective temperature of the primary star (T_1) was set at 6294 K by cross-referencing with Gaia DR2 data (Gaia et al. 2018). We opted for a chain length greater than 40 times the integrated autocorrelation time to guarantee convergence. The light curve underwent 150,000 iterations of the MCMC parameter search post an initial 5000 steps. The final 2000 steps were saved and a corner plot was generated. The posterior distribution of the parameters ($incl, q, f, T_2/T_1, relteff, colat, long, radius$) is showcased in Figure 4. Figure 5 depicts the original light curve using blue dots. The red line in the Figure 5 represents the light curve produced by the model using the derived parameters. The x points on the same panel indicate the light curve generated by Phoebe with identical parameters. The goodness of fit metric (R^2) between the Phoebe-generated light curve using these parameters ($Teff, q, incl, f, T_2/T_1, relteff, colat, long, radius$) and the original light curve stands at 0.989.

The NN_{mol3} model and MCMC algorithm were applied to fit four noteworthy objectives labeled TIC 6171564, TIC 89428764, TIC 93053299, and TIC 97328396. The goodness of fit (R^2) for each of these targets exceeds 0.99. Table 2 outlines the parameters for four contact binaries, while the fitting results for these targets are depicted in Figure 6.

Table 2. The essential parameters of the four contact binary systems

name	T_1 (K)	$incl(\circ)$	σ_{incl}	q	σ_q	f	σ_f	$\frac{T_2}{T_1}$	$\sigma_{\frac{T_2}{T_1}}$	R^2
TIC 671564	5607	81.637	0.443	0.160	0.002	0.668	0.031	1.055	0.006	0.995
TIC 89428764	6541	76.439	0.257	0.136	0.001	0.318	0.022	0.995	0.002	0.999
TIC 93053299	5954	76.706	0.494	0.126	0.002	0.525	0.042	1.020	0.003	0.997
TIC 97328396	5935	86.344	0.469	0.291	0.002	0.502	0.010	1.016	0.002	0.993

The catalog presented in Table 3³ (Columns 1-23) encapsulates the relative parameters and associated uncertainties for 143 contact binaries. Initially, the catalog furnishes foundational data about each target, including target name, orbital period, period uncertainty, and the primary star’s effective temperature (T_1) as derived from Gaia DR2. Subsequently, parameters inferred through neural network (NN_{mol3}) model and Markov Chain Monte Carlo (MCMC) simulations are included. These parameters encompass the orbital inclination ($incl$), mass ratio (q), temperature ratio (T_2/T_1), fill-out factor (f), colatitude ($colat$), longitude ($long$), and angular radius ($radius$), alongside their respective errors. The catalog also features the temperature ratio relative to the local intrinsic value ($relteff$) and its corresponding error.

³ <https://github.com/dingxu6207/Data>

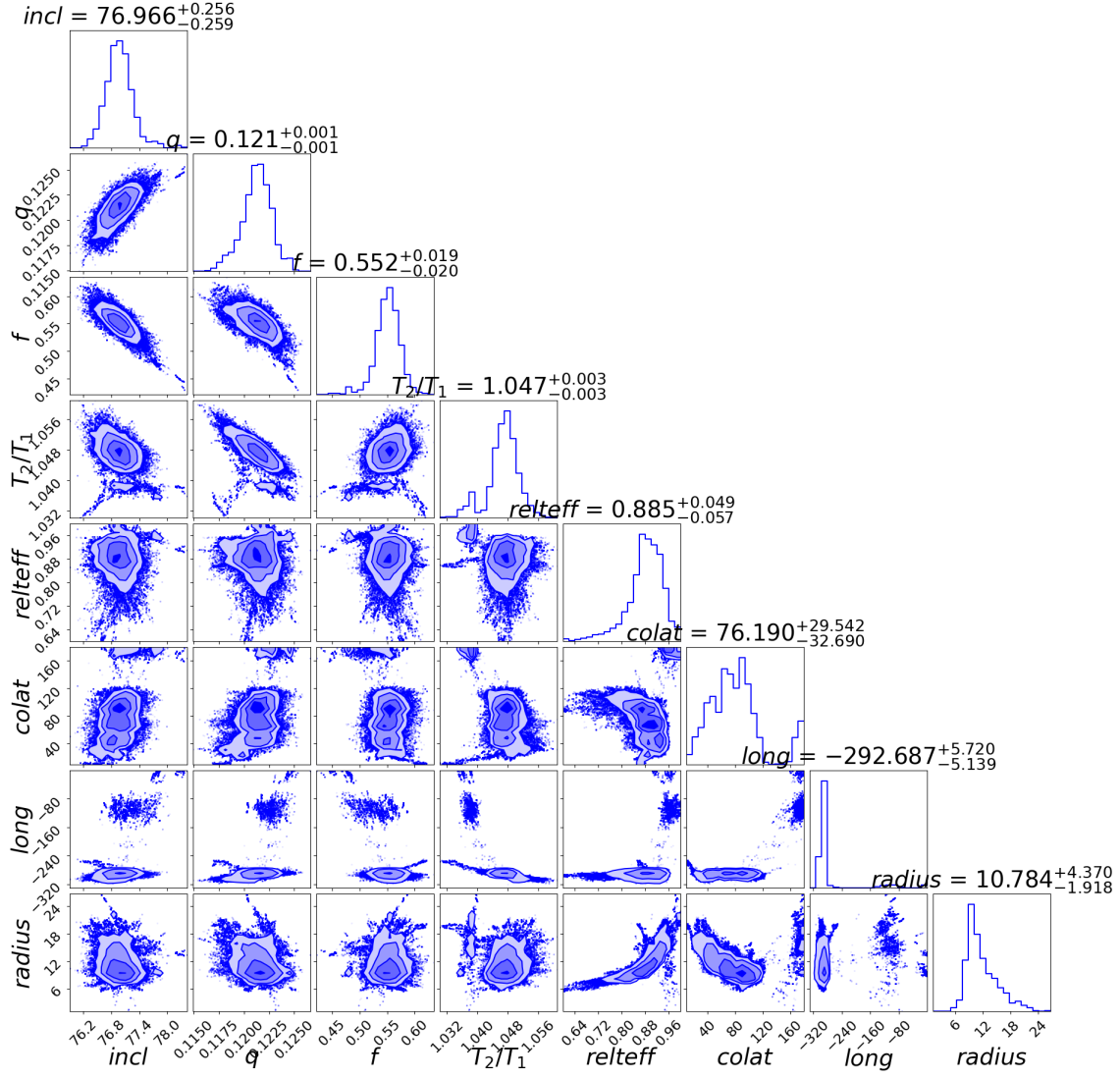


Figure 4. The posterior parameter distributions for TIC 164720673 are presented.

Using the derived parameters, the Phoebe software computes the relative radii of the primary (r_1) and secondary (r_2) stars. This is the equivalent radius in terms of volume. First, calculate the volume of the non-sphere. Then, assume that the equivalent radius refers to the radius of a sphere having the same volume as the non-sphere. The relative radii r_1 and r_2 are the ratios of the primary star's radii to the semi-major axis of the orbit and the secondary star's radii to the semi-major axis of the orbit, respectively. Additionally, the catalog provides the goodness of fit metric (R^2), which quantifies the alignment between the Phoebe-generated light curve and the original observed light curve.

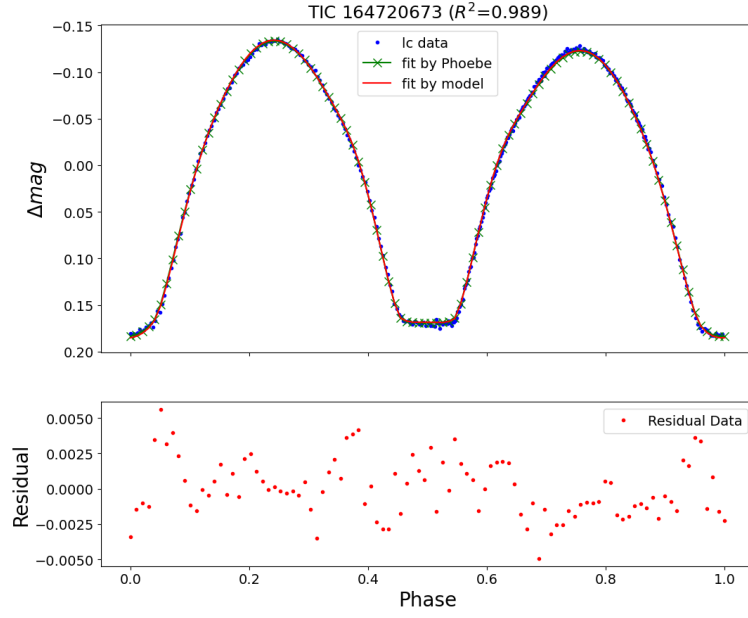


Figure 5. Fitting Results for TIC 164720673 are presented.

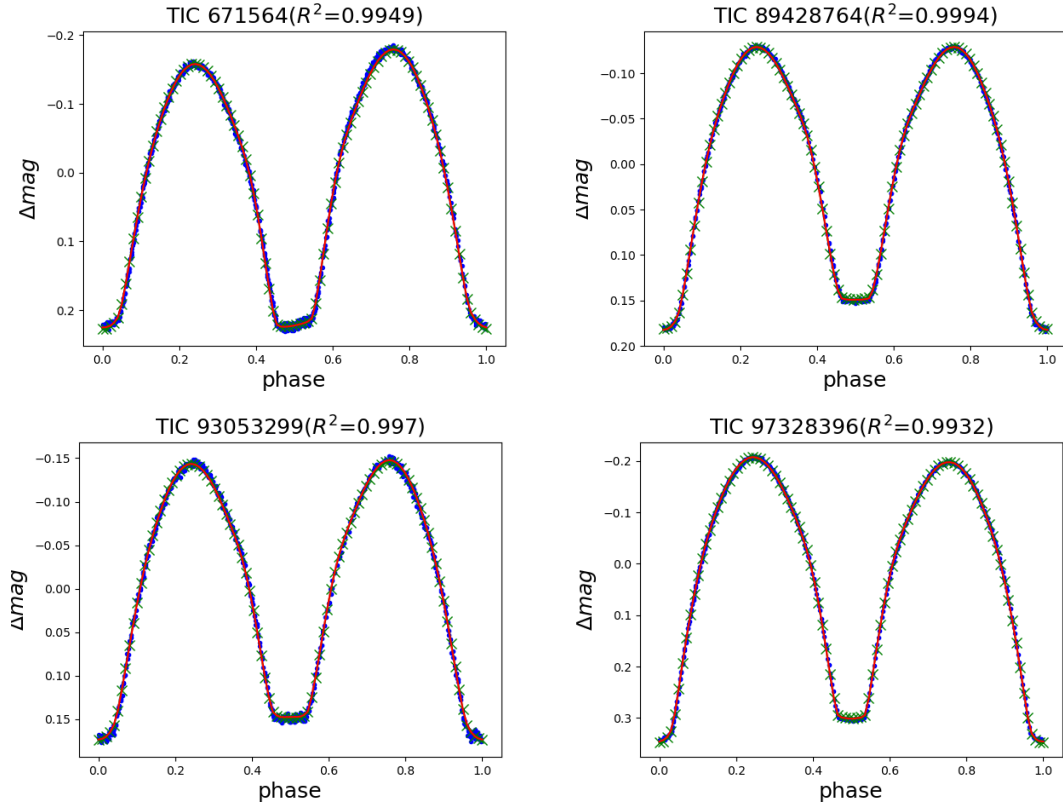


Figure 6. The fitting results for four targets are depicted, with the blue dots indicating the original light curves. The red lines represent the light curves generated by the trained model, and the green x dots denote the light curves produced by Phoebe.

Table 3. Catalog Listing: Fundamental Parameters of 143 Contact Binaries

Num	Column	Units	Explanations
1	name		TESS object name
2	T_1	K	Effective temperature of primary star (from Gaia DR2)
3	Period	day	Orbital period
4	σ_{Period}	day	Uncertainty in Orbital period
5	incl	°	Orbital inclination
6	σ_{incl}	°	Uncertainty in incl
7	q		mass ratio
8	σ_q		Uncertainty in q
9	T_2/T_1		Temperature ratio
10	σ_{T_2/T_1}		Uncertainty in T_2/T_1
11	f		Fill-out factor
12	σ_f		Uncertainty in f
13	$relteff$		Temperature ratio (cool spot)
14	$\sigma_{relteff}$		Uncertainty in $relteff$
15	$colat$		colatitude (cool spot)
16	σ_{colat}		Uncertainty in $colat$
17	$long$		longitude(cool spot)
18	σ_{long}		Uncertainty in $long$
19	$radius$		angular radius (cool spot)
20	σ_{radius}		Uncertainty in $radius$
21	r_1		Relative radii of primary star
22	r_2		Relative radii of secondary star
23	R^2		Goodness of fit
24	a	R_\odot	semi-major axis
25	σ_a	R_\odot	Uncertainty in a
26	M_1	M_\odot	mass of primary star
27	σ_{M_1}	M_\odot	Uncertainty in M_1
28	M_2	M_\odot	mass of secondary star
29	σ_{M_2}	M_\odot	Uncertainty in M_2
30	R_1	R_\odot	radii of primary star
31	σ_{R_1}	R_\odot	Uncertainty in R_1
32	R_2	R_\odot	radii of secondary star
33	σ_{R_2}	R_\odot	Uncertainty in R_2
34	L_1	L_\odot	luminosity of primary star
35	σ_{L_1}	L_\odot	Uncertainty in L_1
36	L_2	L_\odot	luminosity of secondary star
37	σ_{L_2}	L_\odot	Uncertainty in L_2

4.2. Absolute parameters

In the analysis of the catalog referenced in [Latković et al. \(2021\)](#), a total of 153 contact binaries were identified, for which absolute parameters were determined through the combined assessment of their radial velocity and photometric light curves. Notably, all of these contact binaries have temperatures less than 10,000 K. Our findings indicate a strong correlation between the orbital period (P) and the semi-major axis (a), as illustrated in Figure 7. Only one target deviates significantly, named HV UMa ([Csák et al. 2000](#)), with a period of 0.35 days and a semi-major axis of $5.002 R_{\odot}$.

Random Sample Consensus (RANSAC) is a robust iterative algorithm designed to estimate mathematical models from data sets containing outliers ([Dao et al. 2024](#)). By systematically sampling subsets of the data and identifying consensus within these subsets, RANSAC effectively distinguishes between inliers and outliers, thereby enabling a more accurate model estimation. This method is particularly valuable in scientific research, where data quality can be compromised by noise and erroneous measurements, ensuring that the derived models remain reliable and representative of the true underlying relationships. We employed the RANSAC algorithm to remove some outliers and fit an inlier dataset, as shown in Figure 7. The connection between P and a can be expressed using the subsequent linear formula,

$$a = 0.476(\pm 0.053) + 5.687(\pm 0.117) \times P \quad (3)$$

The values of the semi-major axis (a) were calculated based on the orbital period (P). Their respective radii (R_1, R_2) are determined by the semi-major axis (a) and the relative radii (r).

$$R = a \times r \quad (4)$$

The masses of two components were determined using mass ratio (q) and Kepler's third law. G stands for gravitational constant, and P represents the orbital period of system.

$$\frac{a^3}{G(M_1 + M_2)} = \frac{P^2}{4\pi^2} \quad (5)$$

The Stefan-Boltzmann law was employed to calculate the luminosity of the primary star (L_1), followed by the determination of the secondary star's luminosity (L_2).

$$L_1 = R_1^2 \times (4\pi\sigma T_1^4) \quad (6)$$

$$L_2 = R_2^2 \times (4\pi\sigma T_2^4) \quad (7)$$

The calculated parameters include the semi-major axis (a), mass (M_1, M_2), radii (R_1, R_2), and luminosity (L_1, L_2), as presented in Table 3 (Columns 24-37).

The total luminosity ($L_{total} = L_1 + L_2$) obtained in this study was compared with both the luminosity from Gaia DR2 and the one derived from the period-color-magnitude relation. We conduct name matching via Simbad ⁴ and retrieve the parameters from the Gaia DR2 catalog. These parameters encompass parallax (Plx), apparent magnitudes (G, Bp, Rp), proper motions ($pmRA, pmDE$), effective temperature (T_{eff}), and luminosity (Lum). Subsequently, we present a catalog of the relevant Gaia DR2 parameters ³. The period-color-magnitude relation developed and utilized by Rucinski and several collaborators ([Rucinski et al. 1994, 1995, 1997, 2006; Mateo & Rucinski 2017](#)) serves as a highly effective method for estimating the absolute magnitude of W UMa contact binaries. [Mateo & Rucinski \(2017\)](#) have provided a dataset of $M_v = M_v(\log P)$ calibrations for 318 W UMa-type (EW) contact binaries derived from Gaia data. Consequently, initially we can obtain the absolute magnitudes using the formula presented by [Mateo & Rucinski \(2017\)](#) as

$$M_V = 3.73 - 8.67 \times (\log P + 0.4), (0.275 < P < 0.575 \text{ days}) \quad (8)$$

$$M_V = 3.28 - 7.54 \times (\log P + 0.35) + 9.96 \times (\log P + 0.35)^2, (0.22 < P < 0.9 \text{ days}) \quad (9)$$

⁴ <https://simbad.cds.unistra.fr/simbad/>

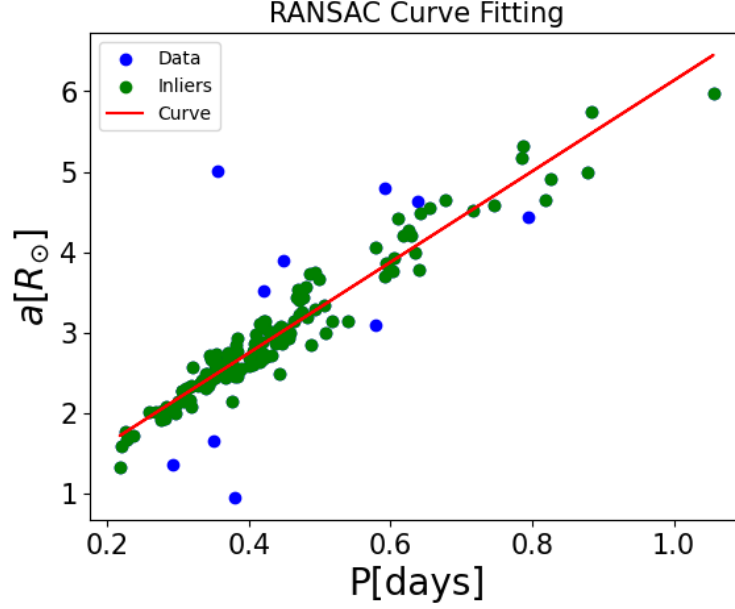


Figure 7. The correlation between the orbital period (P) and the semi-major axis (a) for contact binary systems with temperatures below 10,000 K, as derived from [Latković et al. \(2021\)](#).

Then we can obtain the total luminosity with the relationships as

$$L_{total} = L_1 + L_2 = 10^{-0.4(M_V + BC_v - 4.73)} \times L_{\odot} \quad (10)$$

The bolometric correction (BC_v) is derived using the dataset from [Pecaut & Mamajek \(2013\)](#). The comparison results of the total luminosity (L_{total}) calculations are presented in Figure 8. It can be seen from Figure 8 that the obtained results are linearly correlated, which proves that the method for solving the parameters in this paper is also feasible. The dispersion, when compared with the luminosity from Gaia DR2 as shown in the left panel of Figure 8, is relatively small. The main reason is that the relationship between the semi-major axis (a) and the orbital period (P) is calculated using an empirical formula. The empirical formula shows dispersion, as shown in Figure 7. The dispersion in the right panel of Figure 8 is larger because both the relationship between the semi-major axis (a) and the orbital period (P) and the relationship between the absolute magnitude (M_v) and the orbital period (P) are calculated using empirical formulas. Among the 143 targets, 88 have periods satisfying the range $0.275 < P < 0.575$ days, and 129 meet the criteria of $0.22 < P < 0.9$ days. The comparison results of the L_{total} calculations are presented in Figure 8, with the deviations being $\sigma_{\log(L_{total})} = 0.165$ and $\sigma_{\log(L_{total})} = 0.175$, respectively.

5. DISCUSSION

5.1. Compare another catalog

Through a thorough review of pertinent literature, [Latković et al. \(2021\)](#) performed a statistical and analytical examination of 700 W UMa stars that had been individually analyzed. Our dataset includes 32 entries that correspond with the catalog compiled by [Latković et al. \(2021\)](#), sourced through SIMBAD. We undertook a comprehensive comparison of all 32 overlapping individual objects. The key parameters for these 32 targets are detailed in Table 4. Figure 9 provides a visual comparison of the results showcased in Table 4. The standard deviation of the residuals for the primary star's effective temperature (T_1) across these 32 targets is determined to be 499 K. Similarly, the standard deviation for the orbital inclinations ($incl$) among the same set of targets is found to be 4.05 degrees. For the mass ratios (q), the standard deviation of the residuals is 0.02, while for the fill-out factors (f), it is 0.13. Furthermore, the standard deviation of the residuals for the temperature ratios (T_2/T_1) of these 32 targets is determined to be 0.04. Previous research by [Pribulla et al. \(2003\)](#) has demonstrated that the mass ratios of total eclipsing binaries can be accurately assessed without the necessity of spectroscopic observations. As a result, the mass ratios for such total eclipsing binaries exhibit a notably high level of precision.

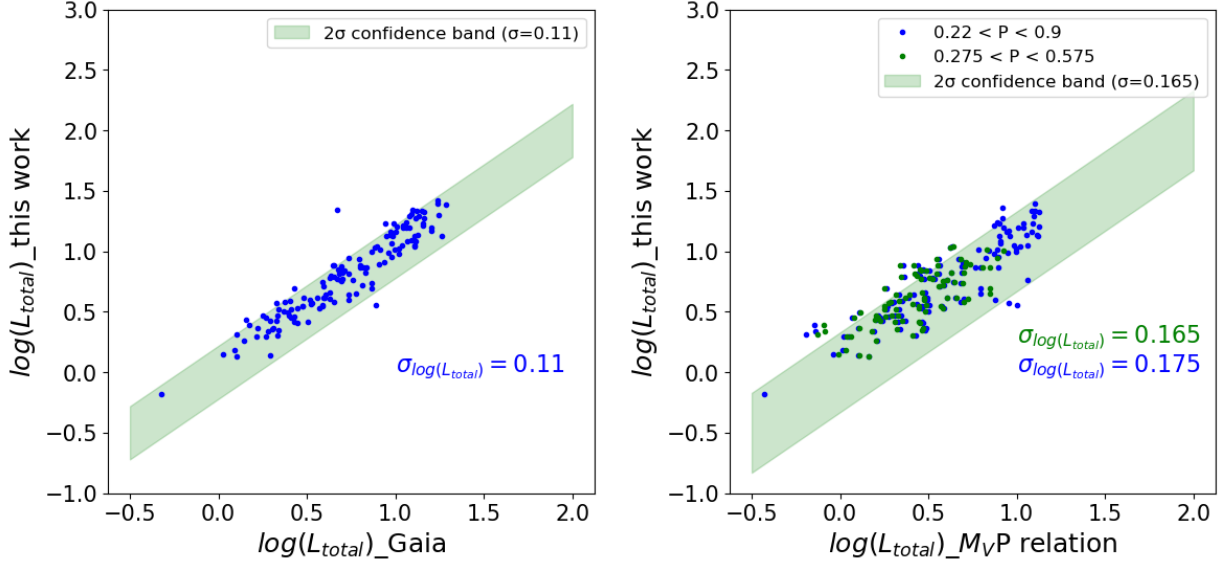


Figure 8. The comparison results of the total luminosity (L_{total}) calculations are presented. The left-hand figure shows the comparison with the luminosity provided by Gaia DR2, while the right-hand figure shows the comparison with the one derived from the period-color-magnitude relation. The blue dots and the light-green dots represent the use of different empirical formulas based on the period.

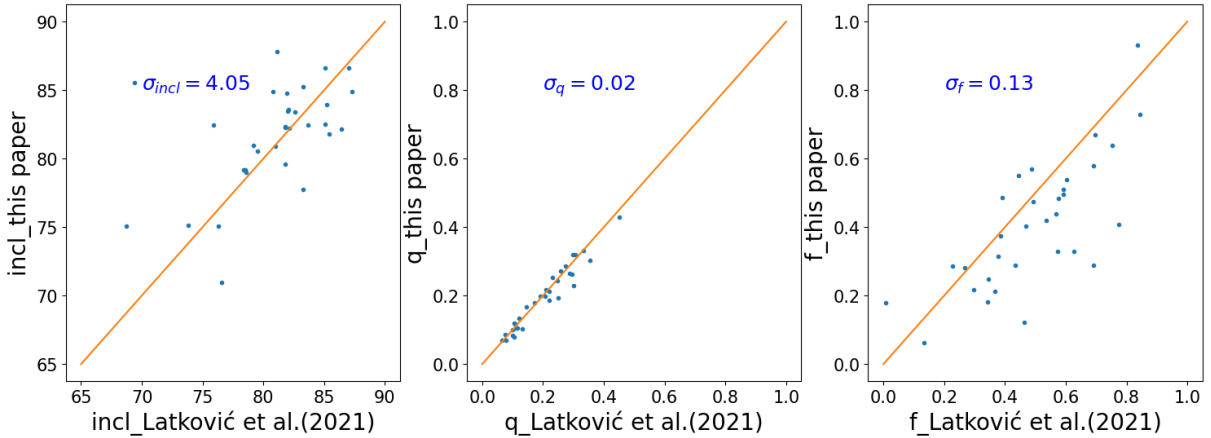


Figure 9. A comparative analysis of the orbital inclination ($incl$), mass ratio (q), and fill-out factor (f) as presented in Table 4. The orange line is the 1:1 line.

For contact binaries displaying flat-bottom minima in their light curves, a notable proportion are classified as systems with low mass ratios. The luminosity of the secondary star is lower, and the spectrum of the system is essentially characterized by the primary star's spectral features. To better illustrate this, we compared the temperatures derived in this study with those obtained from a low-resolution spectroscopic survey conducted using the Large Sky Area Multi-Object Fiber Spectroscopic Telescope (LAMOST) (Luo et al. 2015). We cross-referenced 143 targets with the LAMOST DR11 low-resolution spectra, and LAMOST provided spectroscopic temperature data for 26 of these targets. The standard deviation of the residuals for the effective temperature of the primary star (T_1) across these 26 targets is found to be 376 K in Figure 10.

5.2. New low mass ratio contact binary candidates

Christopoulou et al. (2022) detail the identification and photometric analysis of 30 newly discovered low mass ratio (LMR) totally eclipsing contact binaries with mass ratios $q \leq 0.25$, identified within the data from the Catalina Sky

Table 4. Parameter Comparison: $T_1, incl, q, f, T_2/T_1$ results from this study, $T_1^*, incl^*, q^*, f^*, T_2/T_1^*$ results from [Latković et al. \(2021\)](#).

name	T_1	$incl$	q	f	T_2/T_1	T_1^*	$incl^*$	q^*	f^*	T_2/T_1^*
TIC 144376560	7135	87.820	0.086	0.570	1.082	7410	81.100	0.076	0.487	0.994
TIC 271495349	6688	86.640	0.430	0.375	1.001	6250	87.040	0.452	0.385	0.991
TIC 317470793	5673	86.620	0.332	0.063	0.991	6440	85.100	0.332	0.133	1.000
TIC 170676440	6907	85.530	0.229	0.289	0.870	6881	69.400	0.300	0.691	0.739
TIC 296657504	5769	85.260	0.271	0.183	1.030	5721	83.300	0.257	0.343	1.066
TIC 274967957	5774	84.900	0.261	0.123	0.971	6580	87.310	0.296	0.464	0.952
TIC 417052182	5899	84.870	0.118	0.484	0.994	6215	80.760	0.107	0.577	1.026
TIC 5674169	5874	84.760	0.199	0.473	1.030	5940	81.900	0.190	0.494	0.995
TIC 343409837	6101	83.960	0.105	0.486	1.028	7035	85.200	0.115	0.391	0.950
TIC 157175641	6138	83.580	0.319	0.218	1.027	6014	82.070	0.299	0.298	1.021
TIC 233636431	6896	83.460	0.244	0.249	0.997	6705	81.990	0.248	0.347	0.976
TIC 265015162	5787	83.420	0.118	0.669	1.070	6200	82.600	0.104	0.698	1.051
TIC 359987981	5856	82.510	0.084	0.550	0.997	6640	85.100	0.100	0.446	0.938
TIC 456797644	7019	82.480	0.193	0.728	0.994	6900	83.640	0.250	0.843	1.002
TIC 267043786	6720	82.450	0.304	0.213	0.967	6900	75.890	0.354	0.366	1.021
TIC 294273900	6028	82.310	0.214	0.315	1.047	6383	81.800	0.220	0.378	0.993
TIC 290034099	7810	82.250	0.319	0.402	0.980	6820	81.800	0.306	0.469	0.970
TIC 17563811	6277	82.220	0.099	0.638	1.037	6700	82.100	0.101	0.754	1.016
TIC 372127422	7218	82.160	0.186	0.580	0.991	6900	86.390	0.220	0.693	1.010
TIC 57297550	7038	81.820	0.069	0.931	1.023	8300	85.430	0.065	0.837	1.026
TIC 250203533	5733	80.940	0.167	0.438	1.028	6460	79.190	0.145	0.568	1.032
TIC 411451519	7035	80.900	0.218	0.289	0.982	6912	81.000	0.210	0.434	0.997
TIC 29287800	6125	80.540	0.254	0.287	1.033	6100	79.500	0.232	0.228	1.065
TIC 219738202	6904	79.620	0.265	0.539	0.972	6980	81.800	0.288	0.604	0.968
TIC 458490358	6529	79.200	0.178	0.495	1.020	6500	78.400	0.172	0.592	1.000
TIC 323442776	6116	79.190	0.287	0.282	0.984	6605	78.490	0.275	0.268	0.995
TIC 55753802	6610	78.980	0.198	0.510	1.006	6200	78.600	0.206	0.592	0.998
TIC 13070701	7211	77.770	0.104	0.419	1.000	6347	83.300	0.133	0.535	0.934
TIC 146520491	6484	75.160	0.135	0.330	1.001	6008	73.800	0.120	0.627	0.983
TIC 11480757	7002	75.100	0.104	0.329	1.007	6725	68.710	0.111	0.573	0.920
TIC 103656297	5886	75.100	0.070	0.178	1.041	6100	76.290	0.078	0.008	1.000
TIC 14545690	5883	70.960	0.080	0.407	1.106	5960	76.580	0.106	0.776	1.020

Survey. In this work, [Christopoulou et al. \(2022\)](#) also listed 178 known low mass ratio contact binaries. [Lalounta et al. \(2024\)](#) report the discovery of 7 additional totally eclipsing low mass ratio (LMR) systems derived from the Catalina Sky Surveys (CSS). There are a total of 215 low mass ratio contact binary targets. In our work, we provide a catalog of parameters for 143 totally eclipsing contact binaries, of which 115 have mass ratios $q \leq 0.25$. When we cross-referenced these 115 targets with the previously mentioned 215 objects by SIMBAD, we identified 96 targets not included in the existing catalog, as detailed in Table 5. These 96 objects are likely to represent new low mass ratio contact binary candidates.

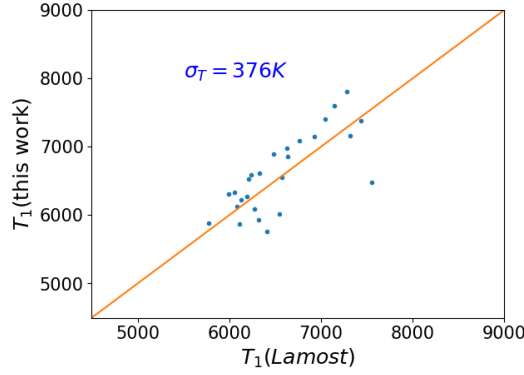


Figure 10. The effective temperatures of the primary star obtained from LAMOST and those derived in this study. The orange line is the 1:1 line.

Table 5. List of 96 Newly Identified Low Mass Ratio Contact Binary Candidates from this study

name	q	name	q	name	q
TIC 103656297	0.070	TIC 114500611	0.152	TIC 11480757	0.104
TIC 115105140	0.164	TIC 115906237	0.129	TIC 116163356	0.151
TIC 123038007	0.149	TIC 138256097	0.232	TIC 140757590	0.182
TIC 141871560	0.168	TIC 142587827	0.156	TIC 143058907	0.081
TIC 428257299	0.117	TIC 432128410	0.157	TIC 434097226	0.248
TIC 436660156	0.210	TIC 43864479	0.176	TIC 439596199	0.108
TIC 441200647	0.108	TIC 450637853	0.154	TIC 452819172	0.143
TIC 453097744	0.194	TIC 392536812	0.085	TIC 393943031	0.152
TIC 398336271	0.122	TIC 399577123	0.147	TIC 400360028	0.070
TIC 401925979	0.167	TIC 401928563	0.118	TIC 402795415	0.160
TIC 406781370	0.150	TIC 411704509	0.187	TIC 415969184	0.134
TIC 336561759	0.164	TIC 339637059	0.087	TIC 348897766	0.219
TIC 354115226	0.229	TIC 356192212	0.113	TIC 365034219	0.212
TIC 36729364	0.234	TIC 377296926	0.158	TIC 380670111	0.108
TIC 38707340	0.137	TIC 387513120	0.167	TIC 387586260	0.225
TIC 198037139	0.135	TIC 257625332	0.217	TIC 289166536	0.242
TIC 332910986	0.181	TIC 426146826	0.090	TIC 293565743	0.100
TIC 29777922	0.095	TIC 314459000	0.186	TIC 315937374	0.136
TIC 316250867	0.192	TIC 316333039	0.116	TIC 316769246	0.143
TIC 320506144	0.097	TIC 330453808	0.155	TIC 258776281	0.154
TIC 260411041	0.121	TIC 261089147	0.232	TIC 261105201	0.128
TIC 261981997	0.105	TIC 268686130	0.175	TIC 279156705	0.155
TIC 279224984	0.159	TIC 199612934	0.091	TIC 204325855	0.245
TIC 211412634	0.175	TIC 233233639	0.107	TIC 237130278	0.145
TIC 250114673	0.093	TIC 255682622	0.082	TIC 257525627	0.197
TIC 156379866	0.143	TIC 159102550	0.220	TIC 164720673	0.121
TIC 170676440	0.229	TIC 193823999	0.223	TIC 47751440	0.112
TIC 49214115	0.164	TIC 53603189	0.142	TIC 55007847	0.086
TIC 56001210	0.227	TIC 5674169	0.199	TIC 63307143	0.154
TIC 63597006	0.142	TIC 66473439	0.091	TIC 671564	0.160
TIC 69838619	0.106	TIC 77178193	0.075	TIC 87751538	0.106
TIC 89428764	0.136	TIC 8989778	0.178	TIC 93053299	0.126

5.3. Estimation of the third light

Hambálek & Pribulla (2024) got an indication of possible third light present in a system. Approximately two-thirds of close binary systems are very likely to be members of triple or multiple star systems (Pribulla et al. 2006). Given this, the effects of the third light cannot be neglected. Therefore, we assume that each target is affected by third light. We consider solving for the mass ratio (q_{l3}) parameter with the inclusion of third light effects and compare it to the mass ratio (q_{nol3}) parameter obtained without considering these effects. In the Phoebe program, the third light is defined as $l_3 = F_3/(F_1 + F_2 + F_3)$. The range of the third light was set from 0 to 1, while all other parameters were maintained as described in Section 3.1. Additionally, a total of 200,000 samples were generated. Similarly, we trained a neural network model (NN_{l3}) to establish the mapping relationship between the parameters and the light curves. We assessed the accuracy of light curves generated by the neural network model (NN_{l3}) by computing the standard deviation of residuals between the model-generated light curves and the synthetic light curves produced by Phoebe across a sample of 20,000 light curves. The left panel of Figure 11 illustrates that the standard deviations of the residuals are predominantly distributed around $0.0003^{+0.0003}_{-0.0001}$. The relative parameters, including the third light (l_3), for 143 contact binaries are determined by employing a neural network (NN_{l3}) model in conjunction with the Markov Chain Monte Carlo (MCMC) algorithm. Table 6 presents the parameters of the targets outlined in Table 2. All 143 targets containing the parameter l_3 , as seen in Table 6, can be found in the GitHub repository³. The mass ratios (q_{nol3} and q_{l3}) for 143 contact binaries, determined using neural network models (NN_{nol3} and NN_{l3}) combined with MCMC algorithms, are compared in the right panel of Figure 11. We calculate the residuals between q_{l3} and q_{nol3} . For these residuals, the first quartile Q_1 (the 25th percentile) is 0.012, the median Q_2 (the 50th percentile) is 0.026, and the third quartile Q_3 (the 75th percentile) is 0.05.

It should be noted that this paper makes the following assumption. All the targets in this study are from total eclipse systems, and the majority of them exhibit low mass ratios. Theoretically, the effective temperature of the primary star measured at the instant when the primary star eclipses the secondary star is the most accurate. Nevertheless, owing to the limitations of the survey data, we are incapable of precisely measuring the effective temperature at this particular moment. Our assumption is to regard the effective temperature of the system as that of the primary star. This is because, for targets with low mass ratios, the luminosity of the system is predominantly contributed by the primary star.

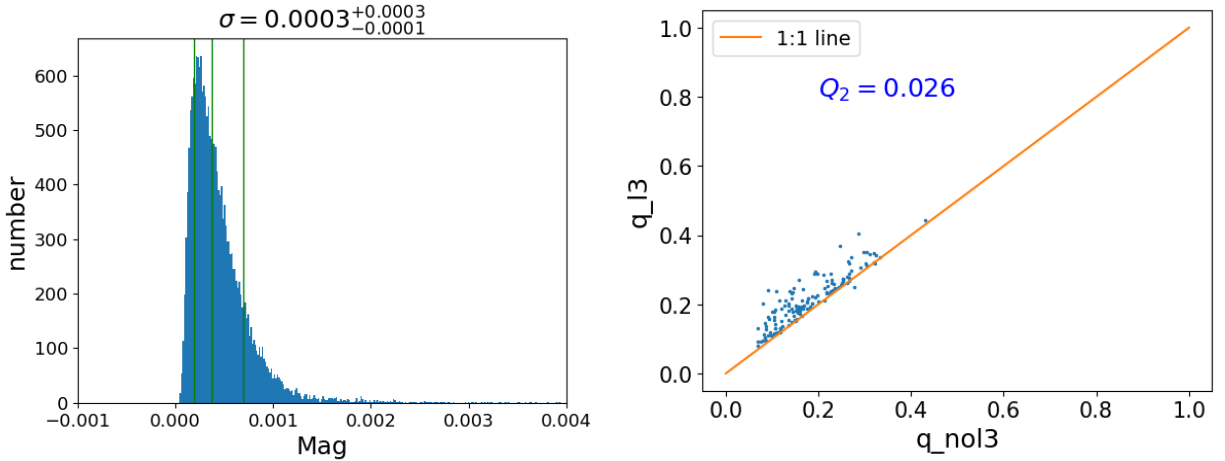


Figure 11. Left: The distribution of the standard deviation of the residuals between the predicted light curves produced by the model (NN_{l3}) and the synthetic light curves produced by Phoebe is depicted. Right: The mass ratios (q_{nol3} and q_{l3}) for 143 contact binaries, determined using neural network models (NN_{nol3} and NN_{l3}) combined with MCMC algorithms, are compared in the right panel.

Table 6. The essential parameters, including the third light (l_3), of the four contact binary systems from the catalog of 143 targets.

name	T_1 (K)	$incl(\circ)$	σ_{incl}	q	σ_q	f	σ_f	$\frac{T_2}{T_1}$	$\sigma_{\frac{T_2}{T_1}}$	l_3	σ_{l_3}	R^2
TIC 671564	5607	83.350	1.635	0.172	0.010	0.744	0.039	1.064	0.004	0.058	0.036	0.995
TIC 89428764	6541	83.130	3.147	0.202	0.022	0.527	0.062	1.000	0.002	0.255	0.058	0.999
TIC 93053299	5954	85.077	3.058	0.196	0.016	0.765	0.069	1.026	0.005	0.277	0.043	0.997
TIC 97328396	5935	88.402	1.132	0.307	0.004	0.519	0.018	1.015	0.003	0.027	0.008	0.993

6. CONCLUSION

Totally eclipsing contact binaries can be accurately characterized through photometric methods alone, allowing for reliable determination of mass ratios without the need for spectroscopic data. We have identified 143 totally eclipsing contact binaries from TESS, whose light curves exhibit flat-bottom minima. The trained neural network (NN_{nol3}) model accurately generates light curves based on input parameters with an error margin of less than 0.001 magnitudes. Using a neural network (NN_{nol3}) model and the MCMC algorithm, we rapidly obtained the fundamental parameters of these contact binaries. By utilizing the relationship between period and semi-major axis using RANSAC algorithm, we estimated the absolute parameters. Low mass ratio systems (LMR) constitute a particularly intriguing category of contact eclipsing binaries that pose significant challenges to current theoretical models of stability. Additionally, these systems are hypothesized to serve as potential progenitors for the rare optical transients known as red novae. Among our catalog, 96 targets have mass ratios below 0.25, not included in previous studies, suggesting that these targets may be newly discovered low mass ratio system candidates. For these targets, we plan to investigate their dynamical instability in future studies and explore their potential for merging. During the parameter estimation of 143 binary systems, we assume the influence of a third light source. A neural network model (NN_{l3}) incorporating this effect is developed. After training NN_{l3} , we calculate the residuals between two mass ratio estimates: q_{l3} (considering the third light) and q_{nol3} (neglecting it). Statistical analysis of these residuals using percentiles shows that the 25th percentile (Q_1) is 0.012, the median (Q_2) is 0.026, and the 75th percentile (Q_3) is 0.05.

In addition, there are still some aspects that demand further in-depth research. In Figure 1, we performed a comprehensive analysis of the O’Connell effect exhibited by the target TIC 103656297. A notable finding was that this effect demonstrates a temporal variation. Looking ahead, we are planning to write a research paper that details the time-dependent variations of the O’Connell effect across 143 targets. When it comes to the data in Figure 9, relying solely on photometric solutions to determine the orbital inclination and fill-out may lead to relatively substantial errors. Moreover, the data presented in Figure 11 regarding the influence of the third light on the mass ratio shows an overall high degree of scatter, which is a cause for concern. To tackle these challenges, in our future research, we intend to integrate spectral radial velocity data, aiming to obtain more accurate and reliable results and gain a more profound understanding of the underlying physical mechanisms.

We are very grateful for the data released by the TESS survey (<https://archive.stsci.edu/missions-and-data/tess/>). This work is supported by the National Key R&D Program of China (Nos. 2022YFF0711500 and 2023YFA1608300), the Strategic Priority Research Programme of the Chinese Academy of Sciences (Grant No. XDB 41000000), the National Natural Science Foundation of China (Nos. 12103088 and 12433009), Yunnan Key Laboratory of Solar Physics and Space Science under No. 202205AG070009, Yunnan Provincial Key Laboratory of Forensic Science (No. YJXK005), Yunnan Basic Research Program (Nos. 202201AU070116 and 202501AT070027), and Yunnan Key Laboratory of Service Computing, Kunming, China. We acknowledge the science research grant from the China Manned Space Project under No. CMS-CSST-2021-A10, No. CMS-CSST-2021- A12, and No. CMS-CSST-2021-B10.

REFERENCES

- Arbutina, B. 2007, MNRAS, 377, 1635
 Arbutina, B. 2009, MNRAS, 394, 501
 Borucki W. J., et al., 2010, Science, 327, 977

- Conroy K. E., Kochoska A., Hey D., Pablo H., Hambleton K. M., Jones D., Giammarco J., et al., 2020, *ApJS*, 250, 34
- Christopoulou P.-E., Lalounta E., Papageorgiou A., Ferreira Lopes C. E., Catelan M., Drake A. J., 2022, *MNRAS*, 512, 1244
- Csák B., Kiss L. L., Vinkó J., Alfaro E. J., 2000, *A&A*, 356, 603
- Dao P., Rast R., Schlaegel W., Schmidt V., Dentamaro A., 2014, *amos.conf*, E55
- Ding X., Song Z., Wang C., Ji K., 2024, *AJ*, 167, 192
- Ding, X., Ji, K., Li, X., et al. 2022, *AJ*, 164, 200
- Efron, R., Yund, E. W., & Divenyi, P. L. 1979, *ASAJ*, 66, 75
- Foreman-Mackey, D., et al. 2019, *J. Open Source Software*, 4, 1864
- Gaia Collaboration, 2018, *A&A*, 616, A1
- Hambálek Ľ., Pribulla T., 2024, *CoSka*, 54, 175.
doi:10.31577/caosp.2024.54.2.175
- K. He, X. Zhang, S. Ren and J. Sun, "Delving Deep into Rectifiers: Surpassing Human-Level Performance on ImageNet Classification," 2015 IEEE International Conference on Computer Vision (ICCV), 2015, pp. 1026-1034, doi: 10.1109/ICCV.2015.123
- Jiang, D., Han, Z., Wang, J., Jiang, T., & Li, L. 2010, *MNRAS*, 405, 2485
- Kuiper G. P., 1941, *ApJ*, 93, 133
- Kopal, Z. 1959, *Close Binary Systems* (New York: Wiley), 127
- Koch D. G., et al., 2010, *ApJ*, 713, L79
- Kingma, D.P., Ba, J., 2014. Adam: A method for stochastic optimization. *arXiv e-prints*, arXiv:1412.6980
- Lomb N. R., 1976, *Ap&SS*, 39, 447
- Lucy, L. B. 1968a, *ApJ*, 151, 1123
- Lucy, L. B. 1968b, *ApJ*, 153, 877
- Lucy L. B., Wilson R. E., 1979, *ApJ*, 231, 502
- Luo, A.-L., Zhao, Y.-H., Zhao, G., et al. 2015, *RAA*, 15, 1095
- Li X.-Z., Liu L., Zhu L.-Y., 2020, *PASJ*, 72, 103
- Li K., Xia Q.-Q., Kim C.-H., Hu S.-M., D.-F. Guo, M.-J. Jeong, Chen X., Gao D.-Y., 2021, *ApJ*, 922, 122
- Latković O., Čeki A., Lazarević S., 2021, *ApJS*, 254, 10
- Li, L., Zhang, F. 2006, *MNRAS*, 369, 2001
- Lalounta E., Christopoulou P.-E., Papageorgiou A., Ferreira Lopes C. E., Catelan M., 2024, *AJ*, 168, 50
- Milone, E. E. 1968, *AJ*, 73, 708
- Marsh, F. M., Prince, T. A., Mahabal, A. A., et al. 2017, *MNRAS*, 465, 4678
- Mateo N. M., Rucinski S. M., 2017, *AJ*, 154, 125
- Mochacki S. W., Doughty N. A., 1972a, *MNRAS*, 156, 51
- Mochacki S. W., Doughty N. A., 1972b, *MNRAS*, 156, 243. doi:10.1093/mnras/156.2.243
- O'Connell, D. J. K. 1951, *PRCO*, 2, 85
- Prša A., Conroy K. E., Horvat M., Pablo H., Kochoska A., Bloemen S., Giammarco J., et al., 2016, *ApJS*, 227, 29.
- Prša A., Guinan E. F., Devinney E. J., DeGeorge M., Bradstreet D. H., Giammarco J. M., Alcock C. R., et al., 2008, *ApJ*, 687, 542
- Pribulla, T., Kreiner, J. M., & Tremko, J. 2003, *CoSka*, 33, 38
- Pribulla T., Rucinski S. M., Lu W., Mochacki S. W., Conidis G., Blake R. M., DeBond H., et al., 2006, *AJ*, 132, 769
- Pecaut M. J., Mamajek E. E., 2013, *ApJS*, 208, 9
- Ricker G. R., Winn J. N., et al., 2015, *JATIS*, 1, 014003
- Rasio, F. A. 1995, *ApJL*, 444, L41
- Rucinski, S. M. 1994, *PASP*, 106, 462
- Rucinski, S. M. 1995, *PASP*, 107, 648
- Rucinski, S. M. 1997, *PASP*, 109, 1340
- Rucinski, S. M. 2006, *MNRAS*, 368, 1319
- Scargle J. D., 1982, *ApJ*, 263, 835
- Sun W., Chen X., Deng L., de Grijs R., 2020, *ApJS*, 247, 50
- Tylenda R., Hajduk M., Kamiński T., Udalski A., Soszyński I., Szymański M. K., Kubiak M., et al., 2011, *A&A*, 528, A114
- Van Hamme, W., & Wilson, R. E. 2007, *ApJ*, 661, 1129
- Wadhwa, S. S., De Horta, A., Filipović, M. D., et al. 2021, *MNRAS*, 501, 229
- Wilson, R. E. 1990, *ApJ*, 356, 613
- Wilson, R. E. 2012, *AJ*, 144, 73
- Wilson, R. E., & Devinney, E. J. 1971, *ApJ*, 166, 605
- Wilson, R. E., Van Hamme, W., & Terrell, D. 2010, *ApJ*, 723, 1469
- Xiong J., Ding X., Li J., Ge H., Cheng Q., Ji K., Han Z., et al., 2024, *ApJS*, 270, 20.
- Yakut K., Eggleton P. P., 2005, *ApJ*, 629, 1055
- Yildiz M., Doğan T., 2013, *MNRAS*, 430, 2029
- Zhao E.-G., Qian S.-B., Zhou X., Li L.-J., Zhu L.-Y., Zhang L., 2021, *MNRAS*, 504, 5155